

ARTICLE OPEN



Directly monitoring the shift in corrosion mechanisms of a model FeCrNi alloy driven by electric potential

Tingkun Liu¹, Cheng-Han Li¹, Matthew Olszta², Jinhui Tao¹✉ and Arun Devaraj¹✉

Stainless steels are used in a myriad of engineering applications, including construction, automobiles, and nuclear reactors. Developing accurate, predictive mechanistic models for corrosion and electrochemical corrosion kinetics of stainless steels has been a topic of research studies over many decades. Herein, we quantified the aqueous corrosion kinetics of a model austenitic Fe–18Cr–14Ni (wt%) alloy in the presence and absence of applied potential using systematic in situ electrochemical atomic force microscopy (EC-AFM) and transmission electron microscopy (TEM). Without an applied bias, vertical dissolution of corrosion pits is controlled by the surface kinetics/diffusion hybrid mechanism, whereas lateral dissolution is diffusion controlled. When an electric bias is applied, the increase in corrosion rate is dominated by the nucleation of new pits. These insights gained by the in situ EC-AFM will allow applications of this method for a quantitative understanding of corrosion of a wider class of materials.

npj Materials Degradation (2023)7:42; <https://doi.org/10.1038/s41529-023-00357-2>

INTRODUCTION

Stainless steels are called “stainless” due to their ability to form a thin protective, chromium oxide layer on the surface¹. Austenitic stainless steels are used as engineering materials in various aggressive environments due to their exceptional corrosion resistance and equally impressive mechanical properties compared to carbon and low-alloy steels. However, when stainless steels are subjected to acidic chloride-containing aqueous environments, with or without an electrochemical bias, severe corrosion can occur^{2–6}. Although chemical corrosion, electrochemical corrosion, and stress-corrosion mechanisms of stainless steels have been the subject of research interest for several decades, the mechanistic understanding based on nanoscale spatially resolved quantitative measurements has only just begun to emerge in the last decade^{7–9}.

For the corrosion study of metallic alloys and steels, in situ atomic force microscopy (AFM) has been widely used to study processes at solid–liquid interfaces due to its high spatial resolution as well as easily changeable solution parameters^{10–12}. For example, the nature and scale of morphological changes at the steel surface during the polishing process have been successfully monitored by in situ AFM¹³. The in situ electrochemical AFM (EC-AFM) can further enable in situ investigation of topographical changes of a sample surface under different electrochemical biases controlled by a potentiostat^{14–17}. Corrosion of metallic alloys and steel under external stress has also been studied using in situ EC-AFM^{18–20}. Besides the research focused on steady-state corrosion reactions of steel, such as the study of pipeline corrosion in bicarbonate solutions or carbonate/bicarbonate electrolytes²¹, the early stages of corrosion have also been investigated, which is important for understanding corrosion initiation. Specifically, in situ EC-AFM in contact mode was used to characterize the early stage of X100 pipeline steel corrosion in bicarbonate solution as a function of solution concentration, which established the relationship between surface roughness and the corrosion process of pipeline steel²². The onset of the corrosion pits on austenitic 304 L stainless steel in chloride borate

buffer solution was studied using in situ EC-AFM in contact mode⁸. This study indicated that grain boundaries (GBs) and surface stoichiometric inhomogeneities significantly enhance the formation of corrosion pits. It also revealed that most pits initiated at strain-hardened areas resulted from mechanical polishing. The preferential corrosion of GBs in a thermally sensitized AISI 304 stainless steel was studied in real time, which showed that an intergranular pit was formed within 0.5 s in 1% sodium chloride (NaCl) solution during a galvanostatic scan using high-speed AFM²³. Above all, AFM has been demonstrated as a powerful method for studying corrosion of steels. To develop reliable models that can accurately predict corrosion kinetics, it is crucial to conduct in situ EC-AFM experiments that are quantitative, nanoscale, and spatially resolved, which provide essential data to better understand the corrosion process and develop robust models that can predict the rate and extent of corrosion under different conditions.

A common type of stainless steel is austenitic stainless steel with a face-centered cubic (FCC) crystal structure. It has been reported that initiation of pitting corrosion and the corrosion susceptibility of the grains are dependent on the crystallographic orientation. It has been shown that the planar orientations, {111} and {100} have the highest resistance to pitting corrosion and generally a lower pitting resistance is expected for the crystallographic planes with lower atomic density of AISI 316LVM stainless steel in 0.1 M NaCl solution with an electric bias²⁴. The dissolution rate and pitting corrosion susceptibilities of different crystallographic planes are also dependent on potentials. For type 310S stainless steel electropolished in sulfuric acid and sodium chloride solution, {100} planes have higher dissolution rate at noble potentials, whereas {111} planes show higher dissolution rate at less noble potentials²⁵. More recently, an in situ AFM study of 316 stainless steels showed that grain-specific corrosion rates decrease as the surface plane progressively deviates from the [111] direction determined by the height changes of individual grains etched in a 0.5 M sulfuric acid and 0.1 M lithium chloride solution up to 80 hours²⁶. The dissolution rate of different

¹Physical and Computational Sciences Directorate, Pacific Northwest National Laboratory, Richland, WA, USA. ²Energy and Environment Directorate, Pacific Northwest National Laboratory, Richland, WA, USA. ✉email: Jinhui.Tao@pnnl.gov; Arun.Devaraj@pnnl.gov

crystallographic planes could be attributed to the anisotropic surface energies, affinities for charged adsorbates, and even electric potentials, which has not been clearly understood yet.

In commercial stainless steels, the presence of multiple alloying elements, impurities, and metallurgical defects often influence the corrosion kinetics. Using a high-purity model Fe–Cr–Ni alloy, a fundamental understanding of the corrosion mechanism can be obtained because it allows elimination of complexity in chemistry and defects. Therefore, in this work, we use *in situ* liquid EC-AFM in combination with *ex situ* aberration, C_s corrected scanning transmission, and transmission electron microscopy (STEM/TEM) analysis before and after corrosion to obtain unprecedented insights into the kinetics of chloride corrosion and subsurface chemical diffusion into the austenite phase in a model Fe alloy sample with 18Cr–14Ni (wt%), which is represented as Fe–18Cr–14Ni.

RESULTS

Microstructure of Fe–18Cr–14Ni alloy

The Fe–18Cr–14Ni alloy contains an equiaxed, random textured grain structure as shown in Fig. 1. The scanning electron microscopy (SEM) backscattered electron image of the microstructure is given in Fig. 1a. The electron backscatter diffraction (EBSD) inverse pole figure (IPF) image in Fig. 1b indicates that the alloy consists of equiaxed grains with extensive annealing twins. The X-ray diffraction (XRD) pattern in Fig. 1c confirmed a fully stabilized FCC structure, indicating that the single austenite phase is present in the alloy.

In situ AFM of the nonbiased sample

The *in situ* AFM images of the nonbiased sample are shown in Fig. 2a–f up to 28.7 min of corrosion. All *in situ* AFM images of the nonbiased sample can be found in Supplementary Fig. 1 in the supporting information. The corrosion pits appeared between 2.2 min and 4.4 min, after which the number of corrosion pits increased, and the size growth of those pits was also analyzed by *in situ* AFM. Six individual pits of the nonbiased sample were selected, as shown in Fig. 2b, to quantitatively characterize the corrosion kinetics. The representative depth and width profiles of Pit #1 and Pit #3 in Supplementary Fig. 2 showed both the depth and the width of these two pits increased as the corrosion time increased. The evolution of depth and width of six individual pits as a function of time is presented in Fig. 2g and h. Within 30 min, the width and depth of these isolated pits continuously increased with corrosion time. The largest growth rate and pit width were found in Pit #1, which is near the GB, as shown in Supplementary Fig. 1. The location of GB is highlighted by the yellow dashed line in Fig. 2a. The sizes and number densities of etching pits at different grains appeared to vary considerably, which could be attributed to the influence of different crystallographic

orientations on the nucleation and corrosion rates. It was also observed that nucleation of the first pit occurred at the GB, and this pit grew into the largest one in the scanned area due to its longer corrosion time and faster corrosion rates. The pit number density in Fig. 2i indicates that pit initiation was fast in the early stage, and there were no new pits formed after 20 min. The evolution of total pitting area in the AFM scanned region is shown in Fig. 2j as a result of pit size (width) and number density.

In situ EC-AFM of the biased sample

Figure 3a–f show topographical images of the biased sample during the *in situ* EC-AFM experiment. All *in situ* AFM images of the biased sample can be found in Supplementary Fig. 4. The AFM scanned region was increased intentionally to include three grains for investigating the effect of crystallographic orientation. The bias was not applied for the first 30 min of corrosion. The first pit was observed at 6.4 min, followed by more pits that appeared and grew as illustrated by the AFM images. Five pits were selected for quantitative kinetic analysis. The evolution of the depth and width of the selected pit is shown in Fig. 3g and h as a function of time. The representative profiles of Pit #3 and Pit #4 are shown in Supplementary Fig. 5. The increase in pit depth was directly proportional to corrosion time. The applied bias did not change the corrosion rate in depth. Interestingly, the pit width reached its maximum after 20 min of corrosion, which was 10 min before the bias was applied. Once the bias was applied, the width of some pits increased and stabilized quickly in several additional minutes. The high pit number density could have limited the pit width from growing, as shown in Fig. 3i. For the selected grains, the highest pit density was found in the [323] oriented Grain #3, which was closest to the [111] orientation. Figure 3h and i both indicate that the applied bias enhanced pit nucleation more significantly than pit width growth. As a result, the corrosion rate in the individual grain is controlled by the pit number density and individual pit width, as shown in Fig. 3j. The red lines of the linear fitting in Fig. 3j indicate the significant increase in total pitting area after the bias was applied. Figure 3j also highlights the highest rate of corrosion in the [323] oriented Grain #3 than in the other two grains. The highest dissolution rate in depth and width was found in Pit #5, which is consistent with the observation of the largest pitting area in the [323] oriented Grain #3.

TEM analysis after corrosion

After the *in situ* AFM corrosion experiments, the structure and composition of corrosion pits in both the nonbiased and biased samples were examined by TEM, as illustrated in Fig. 4. Figure 4a highlights the surface morphology of the sample corroded without bias, forming corrosion pits and individual planar islands in between the corrosion pits. Figure 4b is the dark-field STEM

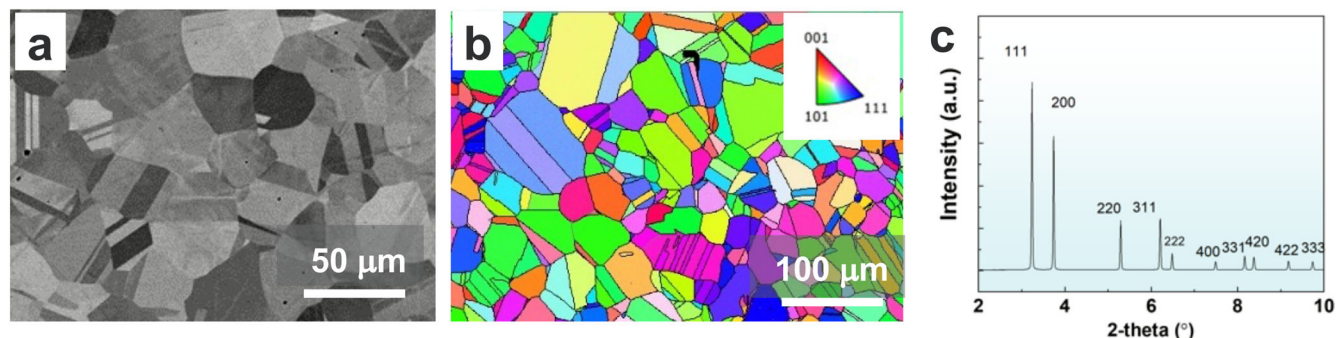


Fig. 1 Microstructure of the annealed Fe–18Cr–14Ni alloy. **a** SEM BSE image, **b** EBSD IPF image, and **c** synchrotron XRD pattern with an X-ray wavelength of 0.1173 Å. The color code of IPF-Z is projected to the surface normal. The diffraction peaks are indexed as a FCC austenite structure.

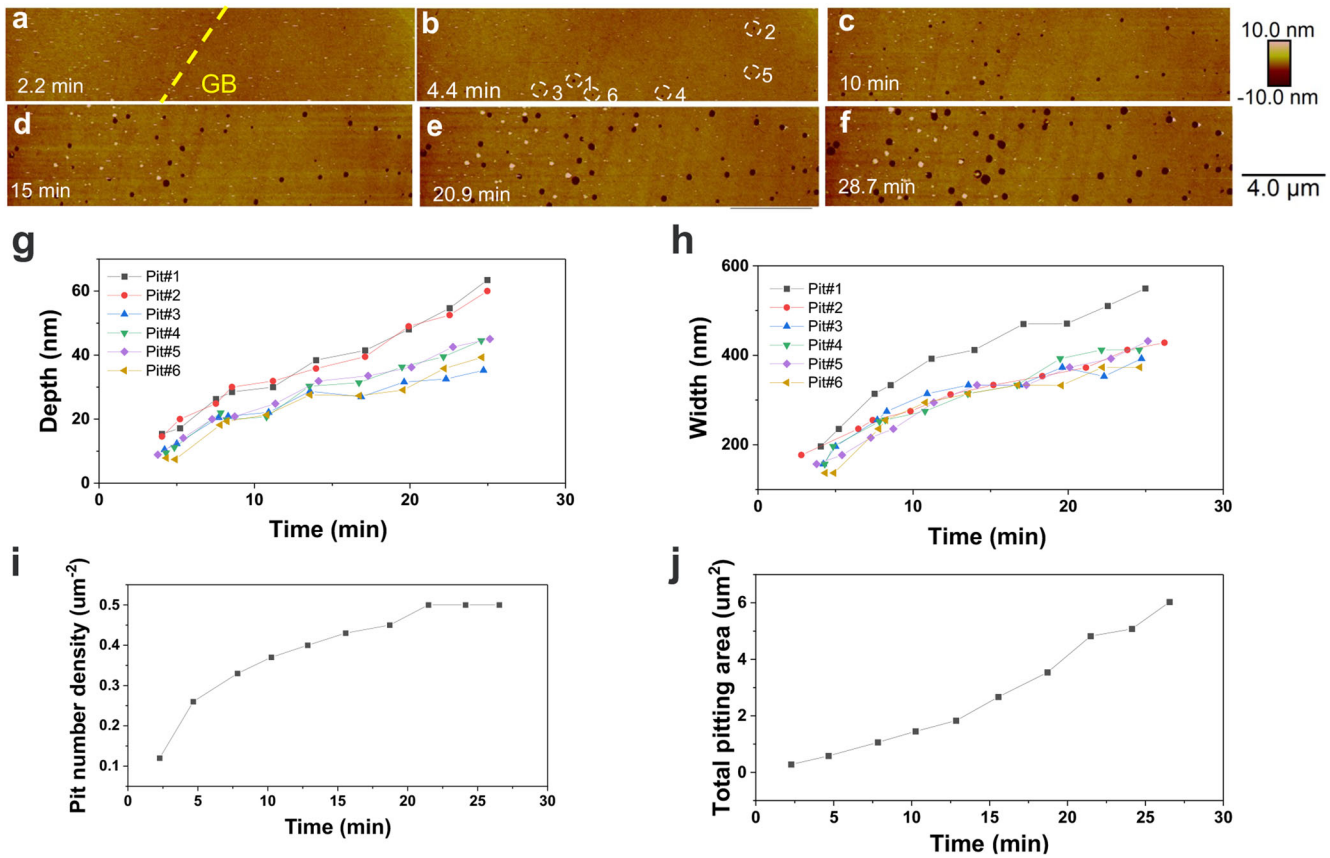


Fig. 2 In situ AFM results of the nonbiased sample. **a–f** In situ EC-AFM topographical images of the nonbiased sample corroded in 0.5 M DCl. Six typical dissolution pits are selected for the quantitative kinetic analysis. Evolution of the **(g)** depth and **(h)** width of an individual pit. Evolution of the **(i)** pit number density and **(j)** total pitting area.

image of a corner between one pit and the island (in the region highlighted by the yellow dashed rectangle in Fig. 4a) where STEM-Energy Dispersive Spectroscopy (EDS) analysis was conducted (Fig. 4c and d, and Supplementary Fig. 7). The STEM-EDS results showed a dual-layer structured oxide scale with an outer Fe-rich oxide layer and an inner Cr-rich oxide layer, with Ni segregation close to the metal–oxide interface. The microstructure of the sample corroded with bias is shown in Fig. 4e. In contrast to the nonbiased sample, the islands in between pits were not observed in the sample corroded with bias. This agrees with the in situ AFM observation of several adjacent pits merging during corrosion with an applied bias. The STEM image and EDS maps of elements from the sample corroded with bias given in Fig. 4f–h and Supplementary Fig. 8 are comparable to what was observed in the sample corroded without bias. The results of composition line scan across the oxide layer can be found in Supplementary Figs. 7 and 8 of the supplementary information. The TEM image in Supplementary Fig. 6 indicated the presence of nano sized Cr₂O₃ grains in the inner oxide layer.

DISCUSSION

The in situ EC-AFM experiments provide nanoscale spatially resolved quantitative analysis of the early-stage corrosion kinetics by characterizing the isolated individual pits. To evaluate the pit growth rate, the depth and width of these isolated pits at different timescales were quantified. For the nonbiased sample, both the depth (Fig. 2g) and width (Fig. 2h) of isolated pits are fitted by a power law with respect to time by $D = \beta_D t^{n_1}$ and $W = \beta_W t^{n_2}$, where D and W are the depth and width of dissolution pits. The constants β_D and β_W are used to evaluate the depth dissolution

rate and width dissolution rate, and n_1 and n_2 are the powers in the kinetics, respectively, as shown in Table 1. The fitting results indicate that the dissolution in depth linearly increased with time ($n_1 = 0.6–0.9$), and Pit #1 exhibited the highest dissolution rate, $\beta_D = 1.68 \pm 0.09 \text{ nm min}^{-n_1}$, among the six selected pits. In contrast, for dissolution along the lateral direction, the power law fitting indicated that the average power n_2 is close to 0.5, despite the slight deviation of Pit #2. The different power values indicate that dissolution along the vertical direction is a surface kinetics/diffusion hybrid controlled due to the power n_1 with the value between 0.5 and 1. Whereas, the dissolution along the lateral directions is diffusion controlled process due to power n_2 of 0.5^{27,28}. Different kinetics of dissolution along various crystallographic orientations has been observed in other inorganic systems such as calcium phosphates^{29,30} and zinc oxide³¹, which was attributed to the varied surface chemistry of crystal faces or different intermediate complex conformations near different step edges. Pit #1 also shows the highest lateral dissolution rate regardless of Pit #2. In a previous study, the linear kinetics were proposed based on the assumption that corrosion is initiated with the removal of the surface passive layer³². However, a linear relationship was proposed between the square of the pit depth and corrosion time, based on the observation of pits growing at the edge of stainless steel foils in chloride solutions³³.

Previous studies^{34–36} have revealed that the surfaces of passive films on stainless steel exist mainly in the form HO–M–HO and that chloride ions adsorb at certain points on the surface to form an intermediate complex^{35,37}, which causes dissolution of the passive film to take place before pit nucleation. From the classical viewpoint of crystal dissolution, when the pit nucleus reaches a critical size, pit growth occurs continuously in these positions

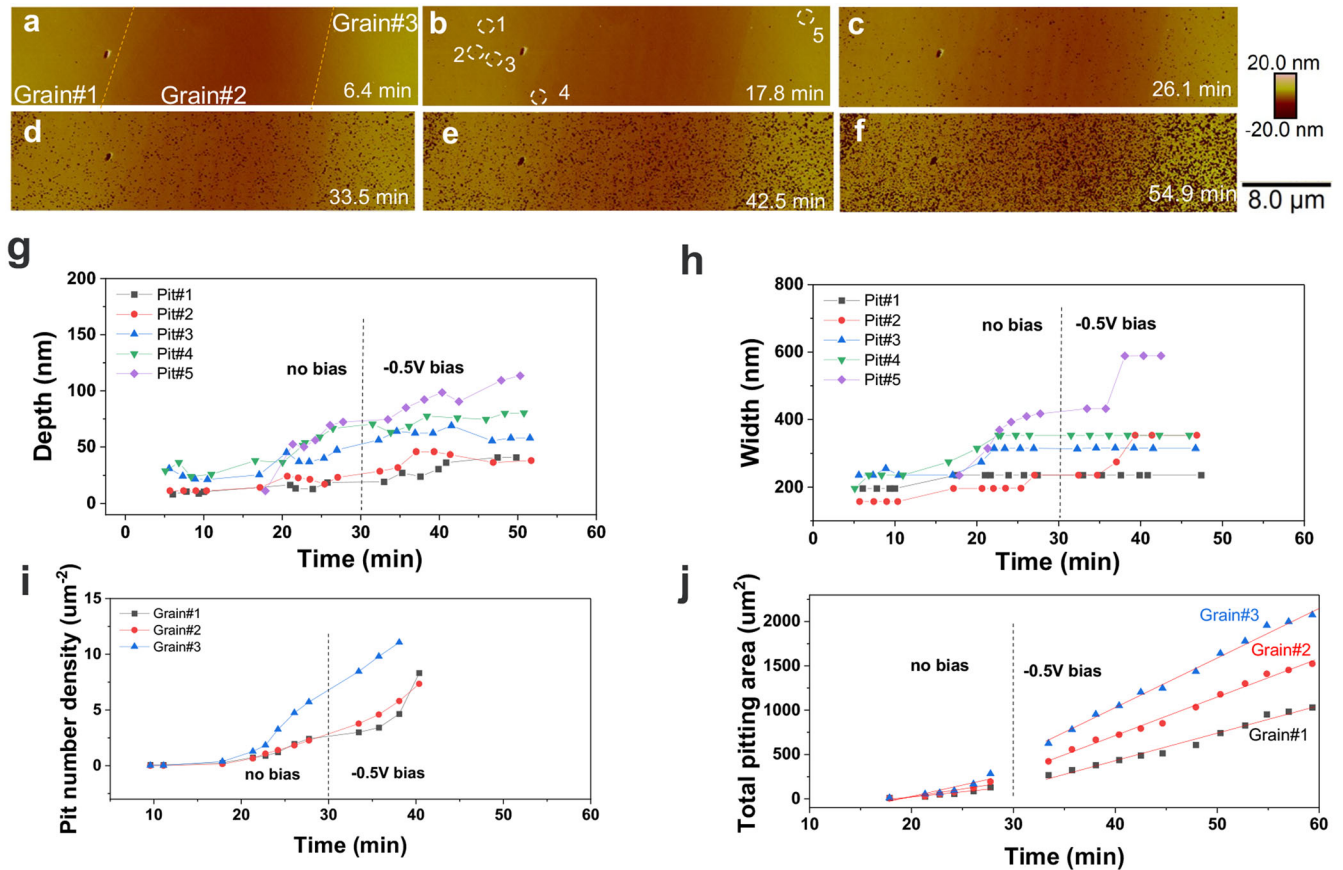


Fig. 3 In situ AFM results of the biased sample. **a–f** In situ EC-AFM topographical images of the biased sample corroded in 0.5 M DCI. The bias was applied after 30 min of corrosion of the sample in DCI. Five pits were selected for the quantitative kinetic analysis. Evolution of the **(g)** depth and **(h)** width of the individual pit. The abrupt increase to a higher width value is due to a merger of the neighboring pits. Evolution of **(i)** pit number density and **(j)** total pitting area in each grain. Three selected grains for quantifying the kinetics are close to the [012] (Grain #1), [124] (Grain #2), and [323] (Grain #3) orientations as shown in Supplementary Fig. 3.

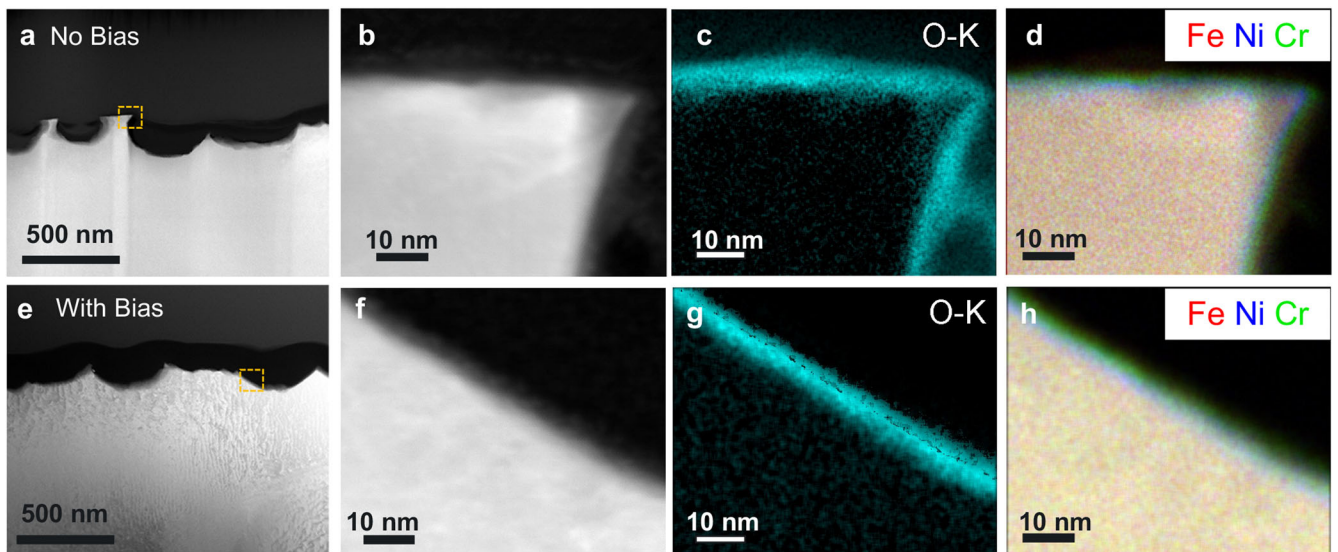


Fig. 4 TEM analysis of corrosion pits. **a** TEM images of nonbiased Fe-18Cr-14Ni after corrosion, highlighting the morphology of pits and a yellow dashed rectangle highlighting a corner region where STEM-EDS analysis was conducted. **b** Higher-magnification dark-field STEM (STEM-DF) image of the corner between one pit and the surface island. EDS map of **(c)** O and **(d)** Fe, Ni, and Cr from the same region. **e** TEM image of the Fe-18Cr-14Ni sample corroded with bias along with a dashed rectangle highlighting the pit where additional STEM-EDS analysis was conducted. **f** STEM-DF image of one pit along with an EDS map of **(g)** O and **(h)** Fe, Ni, and Cr from the same region.

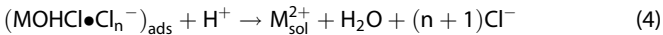
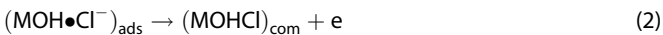
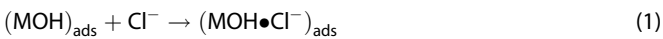
Table 1. Fitting parameters for the nonbiased sample in Pits #1–6 (unit of β_D : nm min⁻¹n₁, unit of β_w : nm min⁻¹n₂, powers n_1 and n_2 are unitless).

	Pit #1	Pit #2	Pit #3	Pit #4	Pit #5	Pit #6
β_D	1.68 ± 0.09	1.95 ± 0.10	1.156 ± 0.14	1.16 ± 0.15	1.28 ± 0.11	0.58 ± 0.06
β_w	4.61 ± 0.07	4.75 ± 0.03	4.55 ± 0.12	4.41 ± 0.07	4.31 ± 0.056	4.16 ± 0.16
n_1	0.743 ± 0.035	0.624 ± 0.039	0.639 ± 0.057	0.828 ± 0.061	0.794 ± 0.044	0.900 ± 0.092
n_2	0.534 ± 0.029	0.391 ± 0.016	0.457 ± 0.049	0.513 ± 0.031	0.540 ± 0.022	0.580 ± 0.065

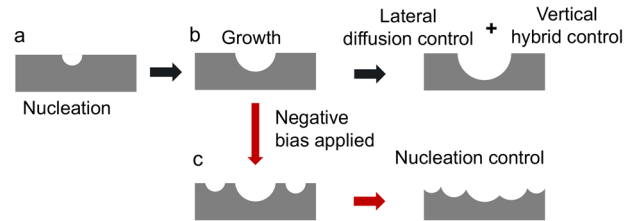
Table 2. Fitting parameters for the biased sample before and after bias was applied in the [012], [124], and [323] grains (unit: $\mu\text{m}^2 \text{min}^{-1}$).

	[012] grain	[124] grain	[323] grain
β_A before bias	11.68 ± 1.94	17.89 ± 3.40	25.49 ± 5.67
β_A after bias	31.05 ± 1.38	43.51 ± 1.25	55.89 ± 1.51

under enough chemical driving force. In areas without Cl⁻ adsorption, the passive layer can remain intact. A mechanism in which chloride ions form an intermediate complex with the passive metal followed by successive dissolution has been proposed in the literature^{35,37}. This type of mechanism composes the following series of processes:



where ads, com, and sol represent adsorbed, complex, and solution species, respectively. Step (2) has been proposed as the rate-controlling step. For lateral dissolution (width direction) at kink site, fewer bonds between the metal atom and its neighbor need to be broken before the release of a metal ion. In contrast, more bonds need to be broken before the release of a metal ion for vertical dissolution (depth direction). Requirement for breaking higher number of bonds corresponds to a slower rate coefficient for the interfacial reaction or detachment of a metal ion during vertical dissolution as showed in Table 1. The corrosion rate is determined by the slowest process in the abovementioned chemical reaction steps (1)–(4), detachment of a metal ion from the etching site, and diffusion of species before and after the reaction. In lateral direction, the observed and fitted results of pit size with corrosion time indicated a diffusion-limited mechanism^{38,39}. This diffusion-limited process indicates that the rates in reaction steps (1)–(4) and detachment of a metal ion from the etching site are relatively faster than the diffusion of species in the lateral direction. Therefore, the resulting metal cations or reactive chloride ion diffusion across in/out across the electrical double layer would most likely be the slowest process compared to reactions (1)–(4) and metal atom detachment from the kink site⁴⁰. In theory, the corrosion rate is possibly controlled by the diffusion rate of metal ions out of a pit, which has been experimentally reported by investigation on one-dimensional (1D) artificial pits^{41,42}. In contrast, in vertical direction, the interfacial reaction or detachment of a metal ion is more similar with the rate of the diffusion of species since this dissolution is the surface kinetics/diffusion hybrid controlled, most likely due to the higher number of bonds that need to be broken before metal ion detachment. Moreover, the highest vertical dissolution rate was found in the pit formed along the GB in the nonbiased sample (Pit #1). This can likely be attributed to the distorted or defective bonding environment of atoms along GBs, which plays an important role

**Fig. 5 Schematic of pitting corrosion.** a pit nucleation; b lateral and vertical growth of individual pits; c nucleation of a new pit due to the applied negative bias and vertical growth of the existing pit.

in interfacial reactions and detachment of metal ions in corrosion processes⁴³.

The biased sample was used to primarily explore the effect of potential on the dissolution mechanism. However, it is shown in Fig. 3g that no obvious change occurred in the vertical dissolution rate after the additional -0.5 V bias was applied. Besides, pit width growth was greatly constrained by the increased pit number density in Fig. 3h and i. The total pitting area in the [012], [124], and [323] grains linearly increased with time by $A = \beta_A t$ both before and after the bias was applied. The values of β_A for the biased case are over two times of those for the nonbiased case, as shown in Table 2. Because both the pit number density and total pit area linearly increase with time, the average pit area should be almost constant. This is consistent with only small changes in the width of the pit, as shown in Fig. 3h. Therefore, the increase in β_A is dominated by nucleation of new pits rather than lateral growth of the existing ones under biased conditions. In comparison, both the nucleation and lateral growth of the pits contribute to the pit area expansion in the nonbiased case (Fig. 2h and i, Fig. 5). This change in the dissolution mechanism could be attributed to shifts in species populations with different charges under negative bias. When the negative potential was applied, the negatively charged species such as Cl⁻ would be less populated and H⁺ would be more populated on the metal surface. The low population of negatively charged species would inhibit reaction steps (1)–(3), which could be an additional reason for termination of lateral pit growth alongside higher pit number density. However, these changes in concentration of ionic surface species promote dissolution by enhancing pit nucleation (Fig. 3i) and keeping the vertical dissolution rate of the existing pits (Fig. 3g), which implies the critical role of H⁺ in reaction step (4) for the nucleation of new pits and vertical dissolution. Similar to the nonbiased case, vertical dissolution under -0.5 V is still hybrid controlled because the chemical reaction or metal ions detachment rates are comparable to the diffusion rate. Tuning of the dissolution mechanism by ionic solution species has been reported before, and the potential bias provides a new knob for this process⁴⁴. Moreover, the material parameters such as crystallographic orientation are also critical to the kinetics of dissolution. The [323] grain shows the highest dissolution rate before and after the bias was applied. The applied negative potential accelerates the dissolution process by promoting the nucleation of a new pit (Fig. 3i). More importantly, the total pitting area was found to linearly increase with time resulting from the combined effect of pit number density and the individual pit

lateral dissolution rate. The in situ EC-AFM results of the biased sample also indicated crystallographic orientation dependent pit growth rate, given the highest area dissolution rate was found in the [323] grain which is close to [111] orientation. Many studies have attributed the dependence of corrosion rates on grain orientation to difference in surface energy^{24,25}. However, the high corrosion rates of [111] grains, which feature a lower surface energy than the [001] and [101] grains, are attributed to their lower tendency to adsorb passivating species from solution, leading to a net reduction in the activation energy of oxidation in austenitic stainless steels²⁶. Future studies will focus on unraveling the corrosion mechanisms for different ionic solution species, sample deformation, and potentials.

In summary, in situ EC-AFM experiments were conducted to study the corrosion kinetics of the Fe–18Cr–14Ni model alloy in DCI solution with and without an applied electrochemical potential. In the nonbiased sample, corrosion along the vertical directions is surface kinetics/diffusion hybrid controlled and corrosion along lateral direction is diffusion controlled processes. The AFM results also indicated that fast dissolution of the pit was initiated along the GB. The corrosion rate in the lateral direction is higher than that in the vertical direction for the nonbiased sample. In the biased sample, the increase in corrosion rate is dominated by nucleation of new pits rather than by lateral growth of existing pits. In comparison, both the nucleation and lateral growth of the pits contribute to corrosion in the nonbiased case. This shift in the dissolution mechanism could be attributed to the redistribution of species with different charges. Additionally, a high corrosion rate was found in the [323] grain, which is close to the [111] orientation. After corrosion, a continuous Cr₂O₃ oxide layer formed, beneath which was a Ni-rich layer. These findings elucidate unprecedented insights into the kinetics of chloride corrosion and subsurface chemical diffusion into the austenite phase. The derivation of the physical relationship, such as pit depth/width vs. corrosion time and pitting area vs. corrosion time in the presence and absence of potential, provides critical experimental proof for further comprehensive understanding of corrosion processes.

This in situ EC-AFM capability for tracking the lateral and vertical dissolution rates of pits both at GBs and in grains with different orientations can now be extended to understanding corrosion of other commercial stainless steels and metal alloys. In addition, the ability to directly correlate EBSD with in situ AFM studies and ex situ TEM analysis can provide in-depth analysis of orientation dependence on pitting corrosion of materials. Understanding such quantitative in situ studies with corrosion kinetic models can be pivotal in enhancing the predictive design of corrosion-resistant metal alloys in the future.

METHODS

Sample preparation and initial microstructure characterization

Fe–18Cr–14Ni alloys were fabricated via arc melting, casting, and homogenizing by remelting five times. The alloys were subsequently cold rolled to 3 mm thick sheets, resulting in a 50% reduction in area, and recrystallized via annealing at 900 °C for 4 h. The microstructure after annealing was characterized by SEM, EBSD, and synchrotron XRD. The samples for in situ AFM were metallographically polished by a vibratory polisher in 0.08 μm colloidal silica for 6 h as the final step. Fiducial marks were put at the corners of regions of interest (ROIs) using a plasma focused ion beam (PFIB) system, and high-resolution EBSD maps were collected from the same ROIs. These ROIs were selected in the center location of the metallography sample where an O-ring was used to confine the liquid solution for in situ EC-AFM experiments. The fiducial marks, SEM, and EBSD imaging were conducted using

a Thermo Fisher Scientific Helios 5 Hydra Dual Beam PFIB-SEM implemented with an Oxford Symmetry EBSD detector. The synchrotron XRD experiment was carried out using an X-ray wavelength of 0.1173 Å at the beamline 11-ID-C of the Advanced Photon Source at Argonne National Laboratory.

In situ EC-AFM experiments

The in situ EC-AFM experiments were performed with a Nanoscope 8 AFM (J scanner, Bruker) at room temperature (~25 °C). The applied three-electrode system contains a Fe–18Cr–14Ni substrate as the working electrode, a platinum wire as the counter electrode, and a leakless Ag/AgCl electrode (ET072 from eDAQ) as the reference. A 0.5 M deuterium chloride (DCI) solution in heavy water (D₂O) was used as the medium. The AFM images were collected via contact mode (Bruker, Nanoscope 8, CA) using hybrid probes consisting of silicon tips on silicon nitride cantilevers (AppNano HYDRA-ALL, spring constant $k = 0.405 \text{ N m}^{-1}$, tip radius <10 nm; <http://www.appnano.com/search-products/HYDRA-ALL>). The images were collected continuously with a scan rate of 1 line/s, with 128 vertical lines per image and the horizontal-to-vertical aspect ratio of 4, and a horizontal size of either 20 or 40 μm to match the marked area characterized by SEM. The images were collected while solution was injected and kept static in a liquid cell. Two samples of the Fe–18Cr–14Ni alloy were prepared for in situ EC-AFM monitoring, denoted as the nonbiased sample and the biased sample in the following content. The sample surface was first imaged in heavy water to find the ROIs before injection of acid for in situ monitoring of corrosion. An area of 5 μm × 20 μm of the nonbiased sample was continuously scanned for a period of about 1.5 h. The biased sample was first corroded in the DCI solution for about 30 min, followed by application of a bias voltage that was then held constant for 1 h. The open circuit voltage was –0.9 V to the reference electrode. An additional –0.5 V bias voltage was applied and kept constant for 1 h. The applied electrochemical bias was controlled using a CH Instrument Model 600E Series Electrochemical Workstation. To cover more grains at the same time, a larger area of 10 μm × 40 μm was continuously scanned for the biased sample. At the end of the experiment, the scan areas were increased to check the behavior at regions outside the scanning area. Zero point in time scale was set to the time when acid was injected into the liquid cell.

Microstructure characterization after in situ corrosion

After in situ EC-AFM, the samples were imaged in SEM to check for surface changes. Site-specific sample preparation followed for STEM/TEM using a dual beam FIB-SEM. STEM/TEM was conducted on an aberration CS corrected JEOL ARM200CF microscope operated at 200 keV. Both a Gatan Orius CCD camera and a Centurio EDS were used to collect images and EDS maps, respectively.

DATA AVAILABILITY

Data used for this manuscript is available from the corresponding authors on request.

Received: 16 November 2022; Accepted: 3 May 2023;

Published online: 24 May 2023

REFERENCES

1. Sedriks, A. J. Corrosion of stainless steels. *Encycl. Mater. Sci. Technol.*, 1707–1708 (2001).
2. Fossati, A., Borgioli, F., Galvanetto, E. & Bacci, T. Corrosion resistance properties of glow-discharge nitrided AISI 316L austenitic stainless steel in NaCl solutions. *Corros. Sci.* **48**, 1513–1527 (2006).

3. Xin, S. & Li, M. Electrochemical corrosion characteristics of type 316L stainless steel in hot concentrated seawater. *Corros. Sci.* **81**, 96–101 (2014).
4. Srinivasan, N. et al. Near boundary gradient zone and sensitization control in austenitic stainless steel. *Corros. Sci.* **100**, 544–555 (2015).
5. Brewick, P. T. et al. Microstructure-sensitive modeling of pitting corrosion: Effect of the crystallographic orientation. *Corros. Sci.* **129**, 54–69 (2017).
6. Li, J. et al. Quantitative 3D characterization for kinetics of corrosion initiation and propagation in additively manufactured austenitic stainless steel. *Adv. Sci.* **9**, 2201162 (2022).
7. Shockley, J. M. et al. Direct observation of corrosive wear by in situ scanning probe microscopy. *ACS Appl. Mater. Interfaces* **12**, 23543–23553 (2020).
8. Martin, F. A., Bataillon, C. & Cousty, J. In situ AFM detection of pit onset location on a 304L stainless steel. *Corros. Sci.* **50**, 84–92 (2008).
9. Hayden, S. C. et al. Genesis of nanogalvanic corrosion revealed in pearlitic steel. *Nano Lett.* **22**, 7087–7093 (2022).
10. Weisenhorn, A. L., Maivald, P., Butt, H. J. & Hansma, P. K. Measuring adhesion, attraction, and repulsion between surfaces in liquids with an atomic-force microscope. *Phys. Rev. B* **45**, 11226–11232 (1992).
11. Tao, J. H., Nielsen, M. H. & De Yoreo, J. J. Nucleation and phase transformation pathways in electrolyte solutions investigated by in situ microscopy techniques. *Curr. Opin. Colloid Interface Sci.* **34**, 74–88 (2018).
12. Birbilis, N., Meyer, K., Muddle, B. C. & Lynch, S. P. In situ measurement of corrosion on the nanoscale. *Corros. Sci.* **51**, 1569–1572 (2009).
13. Abbott, A. P., Capper, G., McKenzie, K. J., Glidle, A. & Ryder, K. S. Electropolishing of stainless steels in a choline chloride based ionic liquid: an electrochemical study with surface characterisation using SEM and atomic force microscopy. *Phys. Chem. Chem. Phys.* **8**, 4214–4221 (2006).
14. Manne, S., Massie, J., Elings, V. B., Hansma, P. K. & Gewirth, A. A. Electrochemistry on a gold surface observed with the atomic force microscope. *J. Vac. Sci. Technol. B* **9**, 950–954 (1991).
15. Reggente, M., Passeri, D., Rossi, M., Tamburri, E. & Terranova, M. L. Electrochemical atomic force microscopy: in situ monitoring of electrochemical processes. *Aip. Conf. Proc.* **1873**, 020009-1-6 (2017).
16. Chen, H. B., Qin, Z. B., He, M. F., Liu, Y. C. & Wu, Z. Application of electrochemical atomic force microscopy (EC-AFM) in the corrosion study of metallic materials. *Materials* **13**, 668 (2020).
17. Hu, Q. et al. The thermodynamics of calcite nucleation at organic interfaces: classical vs. non-classical pathways. *Faraday Discuss* **159**, 509–523 (2012).
18. Padhy, N., Paul, R., Mudali, U. K. & Raj, B. Morphological and compositional analysis of passive film on austenitic stainless steel in nitric acid medium. *Appl. Surf. Sci.* **257**, 5088–5097 (2011).
19. Zhang, X. G. et al. Corrosion behavior of AISI321 stainless steel in an ethylene glycol-water solution. *Int. J. Electrochem. Sci.* **14**, 2683–2692 (2019).
20. Yasakau, K. Application of AFM-based techniques in studies of corrosion and corrosion inhibition of metallic alloys. *Corros. Mater. Degrad.* **1**, 345–372 (2020).
21. Li, Y. & Cheng, Y. F. Passive film growth on carbon steel and its nanoscale features at various passivating potentials. *Appl. Surf. Sci.* **396**, 144–153 (2017).
22. Li, Y. & Cheng, Y. F. In-situ characterization of the early stage of pipeline steel corrosion in bicarbonate solutions by electrochemical atomic force microscopy. *Surf. Interface Anal.* **49**, 133–139 (2017).
23. Moore, S. et al. A study of dynamic nanoscale corrosion initiation events using HS-AFM. *Faraday Discuss.* **210**, 409–428 (2018).
24. Shahryari, A., Szpunar, J. A. & Orriano, S. The influence of crystallographic orientation distribution on 316LVM stainless steel pitting behavior. *Corros. Sci.* **51**, 677–682 (2009).
25. Sato, A., Kon, K., Tsujikawa, S. & Hisamatsu, Y. Effect of crystallographic orientation on dissolution behavior of stainless steels single crystal. *Mater. Trans. JIM* **37**, 729–732 (1996).
26. Dong, S. Q. et al. Elucidating the grain-orientation dependent corrosion rates of austenitic stainless steels. *Mater. Des.* **191**, 108583 (2020).
27. Guo, L. & Searson, P. C. Simulations of island growth and island spatial distribution during electrodeposition. *Electrochem. Solid-State Lett.* **10**, D76–D78 (2007).
28. Guo, L., Oskam, G., Radisic, A., Hoffmann, P. M. & Searson, P. C. Island growth in electrodeposition. *J. Phys. D.* **44**, 443001 (2011).
29. Pan, H. H. et al. Anisotropic demineralization and oriented assembly of hydroxyapatite crystals in enamel: smart structures of biominerals. *J. Phys. Chem. B* **112**, 7162–7165 (2008).
30. Tao, J. H. et al. Structural components and anisotropic dissolution behaviors in one hexagonal single crystal of beta-tricalcium phosphate. *Cryst. Growth Des.* **8**, 2227–2234 (2008).
31. Tao, J. H. et al. Controlling metal-organic framework/ZnO heterostructure kinetics through selective ligand binding to ZnO surface steps. *Chem. Mater.* **32**, 6666–6675 (2020).
32. Paik, J. & Thayamballi, A. Ultimate strength of ageing ships. *Proc. Inst. Mech. Eng., Part M: J. Eng. Marit. Environ.* **216**, 57–77 (2002).
33. Ghahari, M. et al. Synchrotron X-ray radiography studies of pitting corrosion of stainless steel: Extraction of pit propagation parameters. *Corros. Sci.* **100**, 23–35 (2015).
34. Shibata, T. & Okamoto, G. Effect of the Potential of Etching Treatment and Passivation Treatment on the Stability of Passive Stainless Steels. *Corros. Eng. Dig.* **21**, 263–270 (1972).
35. Saadawy, M. Kinetics of pitting dissolution of austenitic stainless steel 304 in sodium chloride solution. *Int. Sch. Res. Notices*, 916367, <https://doi.org/10.5402/2012/916367> (2012).
36. Wang, R. G. et al. Using atomic force microscopy to measure thickness of passive film on stainless steel immersed in aqueous solution. *Sci. Rep.* **9**, <https://doi.org/10.1038/s41598-019-49747-0> (2019).
37. Zhang, P., Wu, J., Zhang, W., Lu, X. & Wang, K. A pitting mechanism for passive 304 stainless steel in sulphuric acid media containing chloride ions. *Corros. Sci.* **34**, 1343–1354 (1993).
38. Scheiner, S. & Hellmich, C. Stable pitting corrosion of stainless steel as diffusion-controlled dissolution process with a sharp moving electrode boundary. *Corros. Sci.* **49**, 319–346 (2007).
39. Nguyen, V. & Newman, R. C. A comprehensive modelling and experimental approach to study the diffusion-controlled dissolution in pitting corrosion. *Corros. Sci.* **186**, 109461 (2021).
40. Galvele, J. R. Transport processes and the mechanism of pitting of metals. *J. Electrochem. Soc.* **123**, 464 (1976).
41. Tester, J. W. & Isaacs, H. S. Diffusional effects in simulated localized corrosion. *J. Electrochem. Soc.* **122**, 1438–1445 (1975).
42. Beck, T. R. & Chan, S. G. Experimental-observations and analysis of hydrodynamic effects on growth of small pits. *Corrosion* **37**, 665–671 (1981).
43. Balluffi, R. W. Grain-boundary diffusion mechanisms in metals. *Metall. Trans. A* **13**, 2069–2095 (1982).
44. Dove, P. M., Han, N. Z. & De Yoreo, J. J. Mechanisms of classical crystal growth theory explain quartz and silicate dissolution behavior. *Proc. Natl Acad. Sci. U.S.A.* **102**, 15357–15362 (2005).

ACKNOWLEDGEMENTS

This research was supported by the U.S. Department of Energy, Office of Science, Basic Energy Sciences program, Materials Sciences and Engineering Division as a part of the Early Career Research program FWP 76052. TEM sample preparation was conducted using facilities at the Environmental Molecular Sciences Laboratory, a Department of Energy (DOE) national user facility funded by the Biological and Environmental Research program and located at Pacific Northwest National Laboratory (PNNL). PNNL is operated by Battelle for DOE under contract DE-AC05-76RL01830.

AUTHOR CONTRIBUTIONS

T.L.: Conceptualization, Methodology, Validation, Formal analysis, Investigation, Writing—original draft. C.-H.L.: Methodology, Writing—review & editing. M.O.: Methodology, Writing—review & editing. J.T.: Conceptualization, Methodology, Supervision, Writing—review & editing. A.D.: Conceptualization, Supervision, Project administration, Funding acquisition, Writing—review & editing.

COMPETING INTERESTS

The authors declare no competing interests.

ADDITIONAL INFORMATION

Supplementary information The online version contains supplementary material available at <https://doi.org/10.1038/s41529-023-00357-2>.

Correspondence and requests for materials should be addressed to Jinhui Tao or Arun Devaraj.

Reprints and permission information is available at <http://www.nature.com/reprints>

Publisher's note Springer Nature remains neutral with regard to jurisdictional claims in published maps and institutional affiliations.



Open Access This article is licensed under a Creative Commons Attribution 4.0 International License, which permits use, sharing, adaptation, distribution and reproduction in any medium or format, as long as you give appropriate credit to the original author(s) and the source, provide a link to the Creative Commons license, and indicate if changes were made. The images or other third party material in this article are included in the article's Creative Commons license, unless indicated otherwise in a credit line to the material. If material is not included in the article's Creative Commons license and your intended use is not permitted by statutory regulation or exceeds the permitted use, you will need to obtain permission directly from the copyright holder. To view a copy of this license, visit <http://creativecommons.org/licenses/by/4.0/>.

© Battelle Memorial Institute 2023